

Variable-temperature lightwave-driven scanning tunneling microscope with a compact, turn-key terahertz source

Cite as: Rev. Sci. Instrum. 95, 023703 (2024); doi: 10.1063/5.0165719

Submitted: 30 June 2023 • Accepted: 26 January 2024 •

Published Online: 20 February 2024



View Online



Export Citation



CrossMark

Hüseyin Azazoglu,^{1,2} Philip Kapitza,^{1,2} Martin Mittendorff,¹  Rolf Möller,^{1,2}  and Manuel Gruber^{1,2,a)} 

AFFILIATIONS

¹ Faculty of Physics, University of Duisburg-Essen, 47057 Duisburg, Germany

² Center for Nanointegration (CENIDE), University of Duisburg-Essen, 47057 Duisburg, Germany

^{a)} Author to whom correspondence should be addressed: manuel.gruber@uni-due.de

ABSTRACT

We report on a lightwave-driven scanning tunneling microscope based on a home-built microscope and a compact, commercial, and cost-effective terahertz-generation unit with a repetition rate of 100 MHz. The measurements are performed in an ultrahigh vacuum at temperatures between 8.5 and 300 K. The cross-correlation of the pump and probe pulses indicates a temporal resolution on the order of a picosecond. In terms of spatial resolution, CO molecules, step edges, and atomically resolved terraces are readily observed in terahertz images, with sometimes better contrast than in the topographic and (DC) current channels. The utilization of a compact, turn-key terahertz-generation system requires only limited experience with optics and terahertz generation, which may facilitate the deployment of the technique to further research groups.

© 2024 Author(s). All article content, except where otherwise noted, is licensed under a Creative Commons Attribution (CC BY) license (<http://creativecommons.org/licenses/by/4.0/>). <https://doi.org/10.1063/5.0165719>

I. INTRODUCTION

Scanning tunneling microscopy (STM) has, since its invention, been a valuable tool to image and probe the properties of individual atoms and molecules adsorbed on surfaces. The transfer of energy and angular momentum between the tunneling electrons and the investigated systems can trigger out-of-equilibrium dynamics, such as the vibration of a molecule,¹ the flipping of a spin,² and the switching of a molecule.³ Because of the limited bandwidth of the trans-impedance amplifiers, conventional STMs can only probe slow dynamics (≥ 1 ms), while effects involving faster dynamics (e.g., spin-flip) are measured in a steady-state regime.

The coupling of terahertz (THz) pulses to the STM junction (hereafter referred to as lightwave-driven STM) provides a sub-picosecond time resolution with negligible thermal effects.^{4–6} A single-cycle THz pulse is generated and transmitted in free space to the STM junction, where the electric field of the THz radiation is enhanced by a factor of 10^5 (Refs. 7–9). The rapidly varying electric field in the junction translates into a transient voltage between the tip and the sample, leading to a transient current. A THz-induced current, I_{THz} , defined as the time-average of the transient current,

is obtained when the transient voltage (of time-average zero) repeatedly sweeps a non-linear region of the current–voltage characteristic. For time resolved measurements, I_{THz} is recorded for varying delays between two THz pulses (pump and probe pulses). Further details may be found in recent reviews.^{5,10} This technique has gained growing interest and has been used, for instance, to track the ultrafast motion of a pentacene molecule,¹¹ to investigate extreme tunnel currents through single atoms on a silicon surface,¹² and to image graphene nanoribbons,¹³ among other recent results.^{14–23} In addition to THz table-top sources, it may be interesting to use intense narrow-band THz pulses from a free electron laser with STM, as it has been done for experiments based on atomic force microscopy.²⁴

The key quantity in lightwave-driven STM (LDSTM) is the average THz-induced current, I_{THz} , which needs to be large enough to be detectable with a high signal-to-noise ratio. I_{THz} essentially depends on the rectification of the THz-induced voltage transient and scales with the repetition rate, f_{Rep} . The reported setups are mostly based on Ti:Sapphire (800 nm) or regenerative ytterbium-doped potassium gadolinium tungstate (Yb:KGW, 1030 nm) lasers with an output powers of 1 W or larger, typically providing pulses with energies between 1 and 40 μJ (see Table I). Tilted-pulse-front

TABLE I. LDSTMs with key parameters related to the generation of the THz pulses. UDE and PCA stand for the University of Duisburg-Essen and photoconductive antenna, respectively.

Location	University of Alberta ⁴		University of Regensburg ¹¹		Yokohama National University ¹⁴		University of Tsukuba ¹⁵		Fritz Haber Institute ¹⁷		University of Stuttgart ²⁰		Michigan State University ¹³		University of California ²²		UDE			
	2013	2016	2018	2019	2020	2021	2021	2021	2021	2021	2021	2021	2021	2021	2021	2022	2022	2023	2023	
Publication year	800	1030	800	1035	800	1032	1035	1035	800	800	1032	1032	1030	1030	820	820	1560	1560	1560	
Laser wavelength (nm)	4	16	...	0.8–40	3	0.5–40	0.8–40	0.8–40	3	3	0.5–40	0.5–40	18	18	1.6×10^{-3}	1.6×10^{-3}	0.2×10^{-3}	0.2×10^{-3}	0.2×10^{-3}	
Energy per optical pulse (μJ)	0.25	0.61	0.001	1–50	1	0.5–41	1–50	1–50	1	1	0.5–41	0.5–41	1	1	1000	1000	100	100	100	
Repetition rate (MHz)	Large area PCA	Lithium niobate	Lithium niobate	Lithium niobate	Spintronic terahertz emitter	Lithium niobate	Lithium niobate	Lithium niobate	Spintronic terahertz emitter	Lithium niobate	Lithium niobate	Lithium niobate	Lithium niobate	Lithium niobate	Plasmonic PCA	Plasmonic PCA	PCA	PCA	PCA	
THz source	THz	THz	THz	THz	THz	THz	THz	THz	THz	THz	THz	THz	THz	THz	THz	THz	THz	THz	THz	THz
Split beam	THz	THz	THz	THz	THz	THz	THz	THz	THz	THz	THz	THz	THz	THz	THz	THz	THz	THz	THz	THz

optical rectification in lithium niobate, the most commonly used for LDSTM, is particularly adapted for the generation of THz pulses with high electric-field amplitudes (1–16 kV/cm). The LDSTM instruments reported so far were, therefore, mostly designed to produce THz pulses of large intensity, thereby sweeping large voltage ranges, on the order of a few volts, of the current–voltage characteristic of the junction. Such large pulses lead to high current densities, reaching 10^{11} A/cm² (Ref. 12), compared to the steady-state regime. Large rectification is achieved in junctions where the current–voltage characteristic, in the range swept by the voltage transient, has a large curvature, for instance, due to electronic states.^{11,12} Conversely, for tunnel junctions with relatively linear current–voltage characteristics, where the rectification is poor, a high repetition rate is required to obtain a measurable signal. So far, the repetition rate of instruments producing a voltage-transient of ≈ 0.1 V is limited to 41 MHz (Ref. 20).²⁵

In addition to the performances, the reported LDSTM instrumentations are generally composed of (i) a large optical table for the laser system and the generation, manipulation, and focusing of the THz pulses, and (ii) a focusing lens in the ultrahigh-vacuum chamber of the STM. Those aspects limit the portability of the THz system.

Here, we report on a lightwave-driven STM instrument based on a home-built STM and a compact, commercial, and cost-effective THz-generation unit with a repetition rate of 100 MHz. The THz system is based on a compact femtosecond erbium fiber laser (1560 nm, 100 mW). To keep the system compact and to circumvent the intensity loss associated with the splitting of THz-pulses, we use a unique design based on *two* photoconductive emitters for the generation of pump and probe THz pulses. The emitters and the focusing mirrors are mounted on a relatively compact, portable plate (20×15 cm²) placed in front of the ultrahigh-vacuum window of the STM at a distance of ~ 15 cm from the STM junction. Measurements at temperatures between 8.5 and 300 K are realized. The cross-correlation of the pump and probe pulses indicates a temporal resolution on the order of a picosecond. In terms of spatial resolution, CO molecules, step edges, and atomically resolved terraces are readily observed in THz images, with often better contrast than in the topographic and (DC) current channels. The high repetition rate of the instrument allows the investigation of junctions with relatively linear current–voltage characteristics, such as metal substrates in the tunneling regime, which is otherwise challenging.¹⁶ The utilization of a compact, turn-key THz-generation system requires very limited experience with optics and THz generation, which may facilitate the deployment of the technique in further STM groups.

II. DESCRIPTION OF THE SETUP

The THz generation and the THz focusing components of our instrumentation are schematized in Fig. 1(a). A compact, turn-key, femtosecond fiber laser (T-Light from Menlo Systems) delivers short pulses (<90 fs) with a center wavelength of 1560 nm at a repetition rate of 100 MHz. A fiber optic splitter splits the pulses into two fibers (0.2 nJ per pulse after split), each of which is connected with an optical fiber to a terahertz photoconductive emitter (Tera15-TX-FC from Menlo Systems) based on InGaAs/InAlAs heterostructures,²⁶ providing an estimated output power of ≈ 30 μW . One of the branches includes a delay line (adapted from Physik

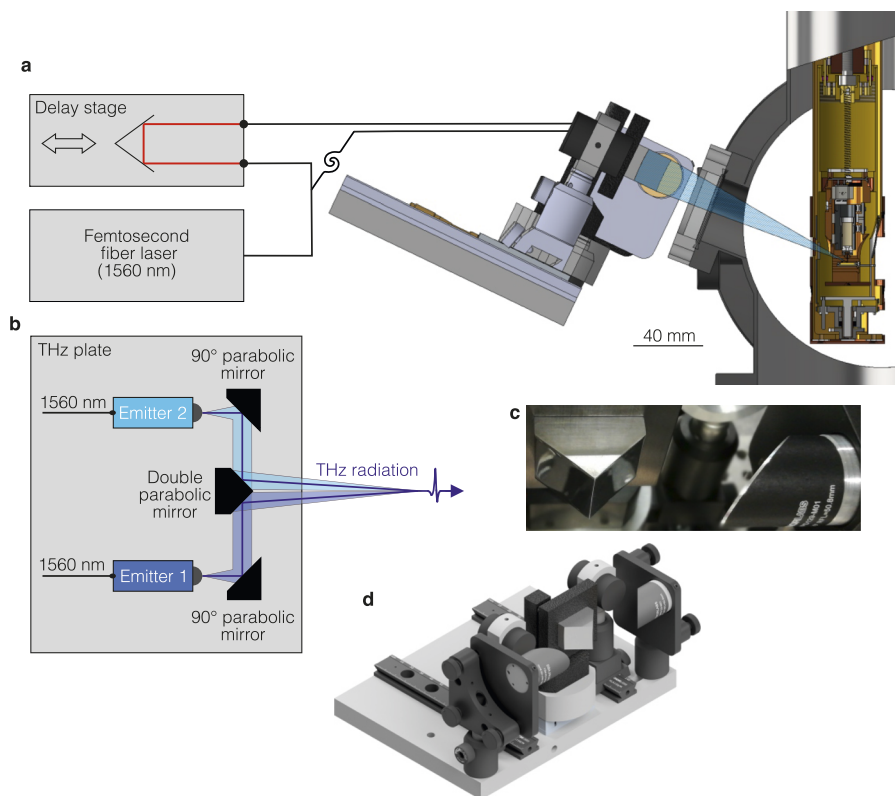


FIG. 1. THz generation and coupling to the STM junction. (a) Overview of the THz-STM setup composed of a femtosecond fiber laser (T-Light from Menlo Systems, a wavelength of 1560 nm), a delay stage (adapted from Physik Instrumente, allowing delays of up to 670 ps), a “THz plate,” and a home-built variable-temperature STM. The angle between the THz beam and the surface normal is 70° . The solid black lines represent optical fibers for the transmission of the 1560 nm-laser light, while the solid red lines depict the laser beam in free space. The delay stage is contained in a box, such that the user is effectively not exposed to beams in the free space. (b) Detail of the THz plate, including two photo-conductive THz emitters (Tera15-TX-FC from Menlo Systems), two 90° off-axis parabolic mirrors, and a double off-axis parabolic mirror (homemade). The main role of this THz plate is to focus the THz radiation from two emitters into a single focal point at the position of the STM junction. (c) Photograph of the double parabolic mirror along with one 90° off-axis parabolic mirror. (d) Three-dimensional view of the THz plate.

Instrumente, delays of up to 670 ps). The transmission in optical fibers allows us to separate the laser system and the delay stage from the STM frame, which would be more difficult for a free-space beam because of the vibrational damping of the STM frame. The two emitters are mounted on a “THz beam combiner plate” [Figs. 1(b) and 1(c)], along with two off-axis parabolic mirrors and a homemade off-axis double parabolic mirror focusing the THz pulses at a distance of 120 mm. The position of the THz plate is adjusted to have the focal point coincide with the STM junction. As the plate is mounted on the same frame as the STM, the vibrational damping of the STM frame does not affect the focus of the THz beam. The generation and focusing of THz pulses are all realized on that plate, which is 20 cm long and 15 cm wide. The femtosecond fiber laser and the delay stage are in a box with dimensions of $56 \times 46 \times 20 \text{ cm}^3$, making the THz-system relatively compact.

It should be mentioned that the usage of two THz emitters, for pump and probe pulses, is so far unique for LDSTMs. This has several advantages compared to a configuration where a single THz beam is split. First, as we generally drive the emitters to their maximum, we reach higher THz-output power. Second, combined

with the double parabolic mirror, it allows us to keep the free-wave THz-path short and keep the system compact.

III. ALIGNMENT OF THE EMITTERS AND MIRRORS

For the alignment of the parabolic mirrors and the characterization of the free-wave THz pulses, the THz-plate is detached from the UHV chamber, deposited on a table, and fixed to an optical rail. A pinhole (0.5 mm diameter) is mounted on the rail at a distance of 120 mm from the double parabolic mirror (Fig. 2). A set of two TPX lenses with a focal length of 50 mm is used to collect and focus the light of the pinhole on a THz detector (Tera15-RX-FC). That detector is triggered by the second output of the laser, which can be delayed using an internal delay line of the laser system. The emitters and mirrors are adjusted to converge the two THz beams to the pinhole. Moreover, the delay between the two independent pulses can be adjusted. The distance between the double parabolic mirror and the pinhole of 120 mm corresponds to the expected distance between the mirror and the STM junction for LDSTM measurements.

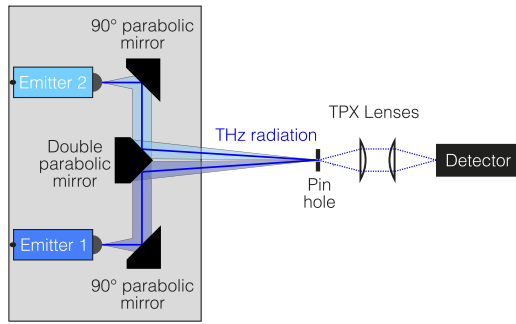


FIG. 2. Set up for the alignment and detection of free-wave THz pulses. The THz plate lies on a table and fixed to an optical rail. A pinhole, two TPX lenses with a focal length of 50 mm, and a THz detector are mounted on that rail. The mirror to pinhole distance is fixed at 120 mm, while the other distances are adjusted to collect and focus the light of the pinhole onto the detector.

Figure 3(a) shows the waveform of the emitted THz pulses as retrieved with the detector after alignment. As expected for electromagnetic waves in free space (without charge), the time integral of the measured signal over one cycle is approximately zero. It should be noted that we do not exactly observe the waveform of the electric field, but the convolution of that waveform with the response function of the detector.

The emitters produce relatively similar THz pulses [compare the red and black curves in Fig. 3(a)], with small variations at ≈ 10 ps. The Fourier spectra are maximum at frequencies of 0.3 THz (emitter 1) and 0.35 THz (emitter 2). The orientations of the emitters have been adjusted such that the polarizations of the THz electric fields are both vertical (leading to p polarization upon coupling to the STM junction). When both emitters are emitting, the total THz electric field at the focal point [green curve in Fig. 3(b) with zero delay between the two pulses] corresponds to the sum of the individual components (dashed black curve).

IV. RECTIFICATION OF THE VOLTAGE TRANSIENT IN THE STM JUNCTION

The THz plate is mounted on the UHV chamber for LDSTM measurements, as shown in Fig. 1 (no THz detector), and the detection is realized via the tunneling current. The detection scheme of LDSTM is essentially the same as previously reported;^{4,11} it is detailed below for pedagogical purposes. The coupling of the THz pulse to the STM junction leads to a transient voltage $v_{\text{THz}}(t)$, whose time integral is zero over one cycle. The induced tunneling current transient is $i_{\text{THz}}(t)$. Figures 4(a)–4(c) illustrate this process for two idealized tunneling junctions with linear (dashed black) and quadratic (blue) current–voltage characteristics. In the case of a linear current–voltage evolution, the THz pulse induces a peak current of ≈ -5 pA [dashed black curve in Fig. 4(b)]. However, the time integral of the current transient, i.e., the net charge flow, is zero [dashed black curve in Fig. 4(c)]. There is no rectification of the voltage transient in a STM junction with a linear current–voltage characteristic. The situation is different when the current in the STM junction evolves quadratically with the voltage. There is a rectification of the voltage transient, which leads to a net charge flow per transient [blue

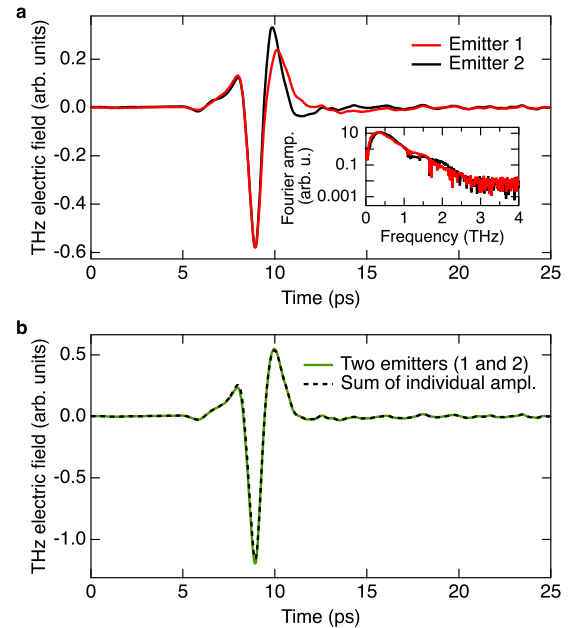


FIG. 3. Lineshapes of the THz pulses in the far field. (a) Electric field transients at the THz focus point generated by emitter 1 (red) and emitter 2 (black). The corresponding Fourier transforms are shown in the inset, which exhibit a maximum at a frequency of ~ 0.3 THz for emitter 1 and 0.35 THz for emitter 2. Emitter 2 is turned off during the data acquisition of emitter 1, and vice versa. (b) THz transient (green) measured at the THz focus point with both emitters active (and no time delay between the generated pulses). The dashed black line is the sum of the individual THz transients [red and black curves in (a)]. The data shown here are not deconvolved from the detector response, such that the actual pulse shape may deviate from these measurements.

curve in Fig. 4(c)]. Note that we here implicitly assumed that the current–voltage characteristic is unaffected by the THz pulse. This is not necessarily the case, but the rectification mechanism remains the same.

Because of the limited bandwidth of the current amplifier of the STM (cutoff frequency of ≈ 1.5 kHz), we are only sensitive to the time-average of i_{THz} ,

$$I_{\text{THz}} = f_{\text{Rep}} \int_0^{1/f_{\text{Rep}}} i_{\text{THz}}(t) \cdot dt, \quad (1)$$

where f_{Rep} is the repetition rate of the THz pulse. I_{THz} is referred to as the THz-induced current. It should be noted that the transient current i_{THz} has a non-zero value for only ≈ 10 ps, such that the time integral in Eq. (1) is independent of the repetition rate ($1/f_{\text{Rep}}$ is typically much larger than one ns). I_{THz} then scales linearly with the repetition rate and indirectly depends on the amplitude of the transient voltage.

I_{THz} is typically small and only represents a small fraction of the total tunneling current. It is, therefore, measured by lock-in detection by chopping the THz beam at ≈ 1 kHz. The chopping is effectively done by modulating the voltage of the emitter electrodes [on/off with a duty cycle of 50%, Fig. 4(d)]. With our repetition rate of 100 MHz, we have on the order of 50 000 THz pulses per modulation cycle (1 ms). The high repetition rate of the laser allows us to

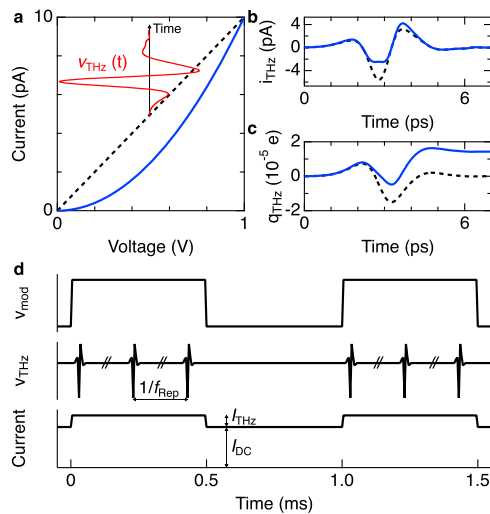


FIG. 4. Illustration of the rectification process. (a) Linear (dashed black) and quadratic (blue) current–voltage characteristics of hypothetical STM junctions. The red waveform depicts a voltage transient induced by the THz pulse, which effectively sweeps the voltage ($V_{DC} = 0.5$ V in this example). Rectified transient (b) current and (c) charge for the two considered current–voltage characteristics. (d) Schematic of the modulation and detection scheme. A square voltage modulation ($f_{mod} \approx 1$ kHz) is applied to the photoemitters. The THz pulses (here for simplicity only the pump pulse) and the corresponding voltage transient v_{THz} are then applied to the junction only when the modulation is in the high state. Note that the duration of the pulses is only about a few picoseconds. The rectification of the THz-induced voltage transients leads to an extra DC current, I_{THz} , when the modulation is in a high state. The tunnel current ($I_{DC} + I_{THz}$) is fed to a lock-in amplifier synchronized with the modulation to extract I_{THz} .

resolve the extra current I_{THz} directly with an oscilloscope in some cases.⁶ Generally, however, I_{THz} is extracted by lock-in detection as it evolves with the same frequency as the chopping of the THz beam [Fig. 4(d)]. Because we are using two independent emitters to generate THz pump and probe pulses, the THz emitters may be chopped individually at different frequencies, or one of the beams, e.g., the pump pulse, may be left non-chopped. For the data shown in the present study, both emitters were chopped with the same modulation voltage.

Following the adjustment of the emitters and mirrors with a THz detector (described above), the fine alignment of the THz beam to the STM junction is done by maximizing the THz-induced current. This is essentially done using precise stepper motors, which displace the whole THz-plate. Finer adjustment of the beam is realized by adjusting the double parabolic mirror with piezo inertia actuators.

Figure 5(a) shows the evolution of the THz-induced current as a function of the amplitude of the THz electric field (characterized in free space) measured on a Ag(111) surface. The evolution is highly non linear (mainly quadratic), as expected because we are sensitive to the rectified current, which depends on the details of the current–voltage characteristics. Because of the relatively linear current–voltage characteristics of Ag(111) at low voltages, we are presumably only rectifying a small fraction of the induced current. The tip–sample distance needs to be extremely small (resistance

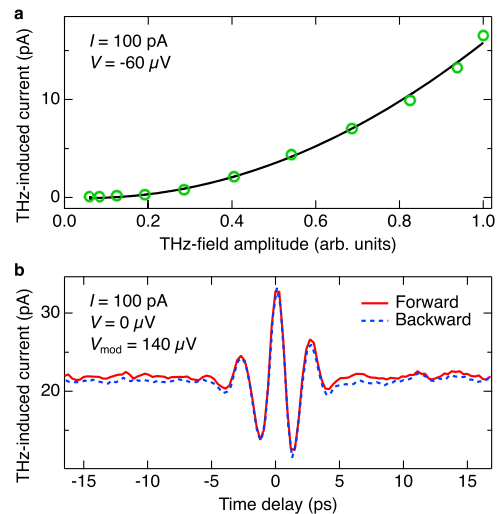


FIG. 5. THz-induced tunneling current on a Ag(111) surface. (a) Evolution of the average THz-induced current as a function of the amplitude of the incoming THz electric field (green circles). The solid line is a quadratic fit to the data (linear term: -1.9 pA, quadratic term: 17.7 pA). (b) THz-induced current as a function of the time delay between the THz pump and probe pulses acquired for increasing (red) and decreasing (blue) delays. A modulation voltage of 140 μ V at 970 Hz was added (we verified that this modulation does not affect the detection of the THz-induced current). The duration of the pulses is on the order of 1 ps, which determines the temporal resolution. Further field-sensitive analysis of the pulse shape can lead to improved temporal resolution. Measurements in (a) and (b) were performed at room temperature with the feedback current loop active (regulating the absolute value of the current).

on the order of 1 M Ω) to have a measurable signal (exponential dependence on the tip–sample distance, as the transient voltage is expected to be independent of the tip–sample distance in the tunneling regime⁹). A typical DC voltage of 1 V would lead to a large current on the order of 1 μ A that would cause issues with stability and surface degradation. We, therefore, use relatively low voltages of ≈ 100 μ V. Under these conditions, the THz-induced current represents $\approx 10\%$ of the total current, which is readily extracted by the lock-in amplifier.

With the repetition rate of our system ($f_{Rep} = 100$ MHz), a THz-induced current of 10 pA corresponds to an average of 0.6 electrons rectified per THz pulse. We are, therefore, in a regime of one to a few electrons per THz pulse on Ag(111) with our instrumentation.

In order to determine the time resolution of the instrument, we use a pair of THz pulses with a variable delay between them. The obtained cross-correlation function for increasing (decreasing) delays is shown in red (blue) in Fig. 5(b). A maximum THz-induced current of 33 pA is obtained for a zero time delay and a minimum of 12 pA for a delay of 1.2 ps. This 1.2 ps represents a higher bound for the time resolution of the system. A similar pump–probe spectrum, measured at the lowest base temperature of 8.5 K, is shown in the Appendix.

V. EXPERIMENTAL RESULTS

We first focus on large images of Ag(111), where the relative height of the tip, the current, and the THz-induced current were

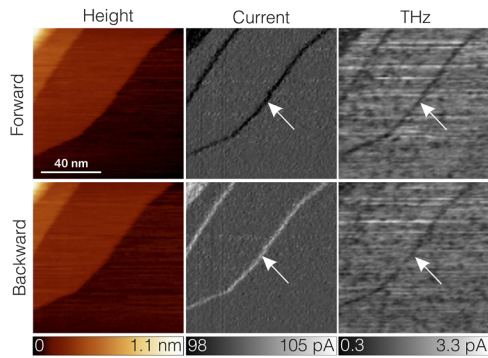


FIG. 6. THz-induced current at step edges. Apparent height (left), average current (middle), and THz-induced current (right) images of a Ag(111) surface for left-to-right (top) and right-to-left (bottom) scan directions. Because of the limited bandwidth of the feedback loop, a height increase (decrease) in the scan direction causes a temporary increase (decrease) of the current (on the order of 1%). In the THz-induced current images, the step edge appears as a depression (the signal decreases by $\approx 25\%$), independently of the scan direction. The arrows point at the same step edge in different images. The images have been acquired at room temperature with $I_{DC} = 100$ pA and $V_{DC} = 250$ μ V at a scanning speed of 24.5 nm/s. These and the following STM images were processed with WSxM.²⁷

simultaneously recorded (Fig. 6). For imaging, we systematically chose a zero time delay between the pump and probe pulses to maximize the signal. The step edges are observed as darker lines in the THz channel (see arrow in the top right image of Fig. 6). A similar signal is observed in the current channel (top center), which is caused by the delayed response of the feedback current loop and the tip-sample distance being too large for a short moment. For the backward image (tip scanning from right to left), the response of the feedback causes an increase in the current (bottom center) due to a temporary too short tip-sample distance. In contrast, the step edges remain darker in the THz image. The darker lines in the THz image, although sensitive (in intensity) to the tip-sample distance, do not exhibit a change of contrast. These lines are, therefore, not directly related to the current. We propose that the I - V characteristic, and in particular $d^2I/dV^2(V)$, of the step edge slightly differ from that of the terrace,²⁸ leading to a different rectification of the THz pulses.

The spatial resolution of the LDSTM is probably better visible in Fig. 7. The atoms of the surface, slightly discernible in the topographic image, can be better observed in the THz image (raw data). This data shows the atomic-resolution capability of the technique and the instrument.

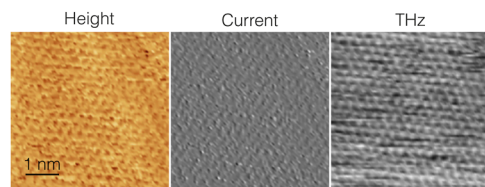


FIG. 7. THz-induced current on a Ag(111) terrace. Apparent height (left), average current (middle), and THz-induced current (right) images of a Ag(111) surface with atomic resolution. The images have been acquired at room temperature with $I_{DC} = 100$ pA and $V_{DC} = -70$ μ V.

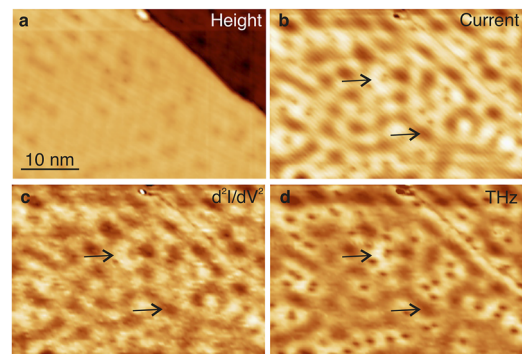


FIG. 8. Impurities, presumably CO molecules, on a Ag(111) surface. (a) Apparent height, (b) average current, (c) d^2I/dV^2 , and (d) THz-induced current images of a Ag(111) surface imaged at 80 K and $V_{DC} = 0$ V ($I_{DC} = 85$ pA). A modulation voltage of 280 μ V at 977 Hz was applied, and d^2I/dV^2 was recorded with a lock-in. The current feedback loop is fed with the absolute value of the current.

To evidence the correlation between the rectification of the tunneling voltage by the non-linear current-voltage characteristic and the THz-induced current, we performed an experiment using a purely AC-tunneling voltage with an amplitude of 280 μ V without a DC-component. Instead of working with the tunneling current directly, the current feedback loop is fed with the absolute value of the current. The observed average tunneling current results from the rectification of the voltage modulation by the tunneling junction. Figure 8 shows the apparent height, average current, d^2I/dV^2 , and the THz-induced current acquired at 80 K on a Ag(111) surface. The surface exhibits ≈ 1 nm wide defects [observed as depressions in Fig. 8(a)], which presumably are CO molecules.²⁹ As $V_{DC} = 0$, the measured average current is sensitive to the non-linearity of the current-voltage characteristic, which rectifies the sinusoidal voltage modulation. To illustrate that, we acquired an image of the second harmonic of the current with a lock-in, which corresponds to $d^2I/dV^2(V = 0)$ [Fig. 8(c)]. The two images are very similar.

The THz-induced current [Fig. 8(d)] is also the result of a voltage rectification, this time not of the modulation voltage but of the repeated voltage transients induced by the THz pulses. The finite d^2I/dV^2 at $V_{DC} = 0$ largely contributes to the rectification of the voltage transient as the modulations of the d^2I/dV^2 signal are visible in the THz image (see, for instance, arrows in Fig. 8 showing areas of larger and smaller intensities). The remaining features of the THz image, for instance, the well-resolved impurities, are likely originating from higher-order derivatives and the larger voltage amplitude of the transient. For completeness, we mention that the backward scan images look identical (not shown).

It appears that the small non-linearity of the current-voltage characteristic induced by surface states and impurities rectifies a (presumably small) fraction of the THz-voltage transients leading to THz images. We carried out additional work on non-linear current-voltage characteristics at larger voltages, which indicate THz-induced voltage amplitudes on the order of a few hundred millivolts. The waveform of the voltage transient remains to be better characterized in future studies.

VI. CONCLUSION

We have developed an ultrahigh-vacuum variable-temperature LDSTM using a compact, commercial, and turn-key THz-generation system based on a cost-effective femtosecond erbium fiber laser. The instrument has a time resolution on the order of one picosecond and a sub-nanometer spatial resolution, providing atomically resolved THz images of a Ag(111) surface. The high repetition rate of the instrument allows probing systems with limited rectification capabilities. The proposed design requires limited experience with optics and the generation of terahertz pulses, which facilitate the deployment of the technique.

ACKNOWLEDGMENTS

We thank Tobias Roos, Detlef Utzat, and Doris Tarasevitch for their technical support. This work was funded by the Deutsche Forschungsgemeinschaft (DFG, German Research Foundation) Project No. 278162697-SFB 1242.

AUTHOR DECLARATIONS

Conflict of Interest

The authors have no conflicts to disclose.

Author Contributions

Hüseyin Azazoglu: Formal analysis (equal); Investigation (equal); Methodology (equal); Visualization (equal); Writing – review & editing (equal). **Philip Kapitza:** Investigation (supporting). **Martin Mittendorff:** Methodology (equal); Writing – review & editing (supporting). **Rolf Möller:** Conceptualization (equal); Formal analysis (equal); Funding acquisition (equal); Investigation (equal); Methodology (equal); Supervision (equal); Writing – review & editing (equal). **Manuel Gruber:** Funding acquisition (equal); Investigation (equal); Methodology (equal); Supervision (lead); Visualization (equal); Writing – original draft (lead).

DATA AVAILABILITY

The data that support the findings of this study are available from the corresponding author upon reasonable request.

APPENDIX: PUMP-PROBE MEASUREMENTS AT 8.5 K

A z-cut quartz window (Korth Kristalle GmbH) of a thickness of 2 mm is fixed on the opening of the outer radiation shield

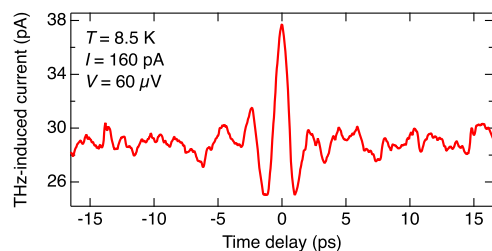


FIG. 9. THz-induced current as a function of the time delay between the THz pump and probe pulses acquired on Ag(111) at 8.5 K.

($\approx 1 \text{ cm}$ in diameter) to prevent cryopumping onto the sample and to limit the thermal radiation toward the STM. The lowest base temperature of our instrument is 7.5 K (shields fully closed), which is increased to 8.5 K during LDSTM measurements. Figure 9 shows an example of a THz pump-probe measurement performed at this lowest temperature.

REFERENCES

- 1 B. C. Stipe, M. A. Rezaei, and W. Ho, "Single-molecule vibrational spectroscopy and microscopy," *Science* **280**, 1732–1735 (1998).
- 2 A. J. Heinrich, J. A. Gupta, C. P. Lutz, and D. M. Eigler, "Single-atom spin-flip spectroscopy," *Science* **306**, 466–469 (2004).
- 3 Y. Kim, K. Motobayashi, T. Frederiksen, H. Ueba, and M. Kawai, "Action spectroscopy for single-molecule reactions—Experiments and theory," *Prog. Surf. Sci.* **90**, 85–143 (2015).
- 4 T. L. Cocker, V. Jelic, M. Gupta, S. J. Molesky, J. A. J. Burgess, G. D. L. Reyes, L. V. Titova, Y. Y. Tsui, M. R. Freeman, and F. A. Hegmann, "An ultrafast terahertz scanning tunnelling microscope," *Nat. Photonics* **7**, 620–625 (2013).
- 5 T. L. Cocker, V. Jelic, R. Hillenbrand, and F. A. Hegmann, "Nanoscale terahertz scanning probe microscopy," *Nat. Photonics* **15**, 558–569 (2021).
- 6 H. Azazoglu, R. Moller, and M. Gruber, "Thermal expansion in photo-assisted tunneling: Visible light versus free-space terahertz pulses," *arXiv:2311.15557* (2023).
- 7 J. H. Kang, D. S. Kim, and Q.-H. Park, "Local capacitor model for plasmonic electric field enhancement," *Phys. Rev. Lett.* **102**, 093906 (2009).
- 8 D. Peller, "Femtosecond videography and control of single-molecule dynamics with atom-scale lightwaves," Ph.D. thesis, Universität Regensburg, 2020.
- 9 D. Peller, C. Roelcke, L. Z. Kastner, T. Buchner, A. Neef, J. Hayes, F. Bonafé, D. Sidler, M. Ruggenthaler, A. Rubio, R. Huber, and J. Repp, "Quantitative sampling of atomic-scale electromagnetic waveforms," *Nat. Photonics* **15**, 143–147 (2021).
- 10 T. Tachizaki, K. Hayashi, Y. Kanemitsu, and H. Hirori, "On the progress of ultrafast time-resolved THz scanning tunneling microscopy," *APL Mater.* **9**, 060903 (2021).
- 11 T. L. Cocker, D. Peller, P. Yu, J. Repp, and R. Huber, "Tracking the ultrafast motion of a single molecule by femtosecond orbital imaging," *Nature* **539**, 263–267 (2016).
- 12 V. Jelic, K. Iwaszczuk, P. H. Nguyen, C. Rathje, G. J. Hornig, H. M. Sharum, J. R. Hoffman, M. R. Freeman, and F. A. Hegmann, "Ultrafast terahertz control of extreme tunnel currents through single atoms on a silicon surface," *Nat. Phys.* **13**, 591–598 (2017).
- 13 S. E. Ammerman, V. Jelic, Y. Wei, V. N. Breslin, M. Hassan, N. Everett, S. Lee, Q. Sun, C. A. Pignedoli, P. Ruffieux, R. Fasel, and T. L. Cocker, "Lightwave-driven scanning tunnelling spectroscopy of atomically precise graphene nanoribbons," *Nat. Commun.* **12**, 6794 (2021).
- 14 K. Yoshioka, I. Katayama, Y. Arashida, A. Ban, Y. Kawada, K. Konishi, H. Takahashi, and J. Takeda, "Tailoring single-cycle near field in a tunnel junction with carrier-envelope phase-controlled terahertz electric fields," *Nano Lett.* **18**, 5198–5204 (2018).
- 15 S. Yoshida, H. Hirori, T. Tachizaki, K. Yoshioka, Y. Arashida, Z.-H. Wang, Y. Sanari, O. Takeuchi, Y. Kanemitsu, and H. Shigekawa, "Subcycle transient scanning tunneling spectroscopy with visualization of enhanced terahertz near field," *ACS Photonics* **6**, 1356–1364 (2019).
- 16 Y. Luo, V. Jelic, G. Chen, P. H. Nguyen, Y.-J. R. Liu, J. A. M. Calzada, D. J. Mildenerberger, and F. A. Hegmann, "Nanoscale terahertz STM imaging of a metal surface," *Phys. Rev. B* **102**, 205417 (2020).
- 17 M. Müller, N. Martín Sabanés, T. Kampfrath, and M. Wolf, "Phase-resolved detection of ultrabroadband THz pulses inside a scanning tunneling microscope junction," *ACS Photonics* **7**, 2046–2055 (2020).
- 18 D. Peller, L. Z. Kastner, T. Buchner, C. Roelcke, F. Albrecht, N. Moll, R. Huber, and J. Repp, "Sub-cycle atomic-scale forces coherently control a single-molecule switch," *Nature* **585**, 58–62 (2020).

- ¹⁹S. Yoshida, Y. Arashida, H. Hirori, T. Tachizaki, A. Taninaka, H. Ueno, O. Takeuchi, and H. Shigekawa, "Terahertz scanning tunneling microscopy for visualizing ultrafast electron motion in nanoscale potential variations," *ACS Photonics* **8**, 315–323 (2021).
- ²⁰M. Abdo, S. Sheng, S. Rolf-Pissarczyk, L. Arnhold, J. A. J. Burgess, M. Isobe, L. Malavolti, and S. Loth, "Variable repetition rate THz source for ultrafast scanning tunneling microscopy," *ACS Photonics* **8**, 702–708 (2021).
- ²¹S. Sheng, A.-C. Oeter, M. Abdo, K. Lichtenberg, M. Hentschel, and S. Loth, "Launching coherent acoustic phonon wave packets with local femtosecond Coulomb forces," *Phys. Rev. Lett.* **129**, 043001 (2022).
- ²²L. Wang, Y. Xia, and W. Ho, "Atomic-scale quantum sensing based on the ultrafast coherence of an H₂ molecule in an STM cavity," *Science* **376**, 401–405 (2022).
- ²³S. Chen, W. Shi, and W. Ho, "Single-molecule continuous-wave terahertz rectification spectroscopy and microscopy," *Nano Lett.* **23**, 2915–2920 (2023).
- ²⁴S. Kehr, Y. Liu, L. Martin, P. Yu, M. Gajek, S.-Y. Yang, C.-H. Yang, M. Wenzel, R. Jacob, H.-G. Von Ribbeck, M. Helm, X. Zhang, L. Eng, and R. Ramesh, "Near-field examination of perovskite-based superlenses and superlens-enhanced probe-object coupling," *Nat. Commun.* **2**, 249 (2011).
- ²⁵A repetition rate of 1 GHz was reported in Ref. 22 providing a peak voltage of 4.2 mV, which limits the applicability to low-energy excitation.
- ²⁶R. J. B. Dietz, D. Stanze, H. Roehle, M. Koch, and T. Go, "64 μ W pulsed terahertz emission from growth optimized InGaAs/InAlAs heterostructures with separated photoconductive and trapping regions," *Appl. Phys. Lett.* **103**, 061103 (2013).
- ²⁷I. Horcas, R. Fernández, J. M. Gómez-Rodríguez, J. Colchero, J. Gómez-Herrero, and A. M. Baro, "WSXM: A software for scanning probe microscopy and a tool for nanotechnology," *Rev. Sci. Instrum.* **78**, 013705 (2007).
- ²⁸J. Li, W.-D. Schneider, and R. Berndt, "Local density of states from spectroscopic scanning-tunneling-microscope images: Ag(111)," *Phys. Rev. B* **56**, 7656–7659 (1997).
- ²⁹M. Kulawik, H.-P. Rust, M. Heyde, N. Nilius, B. Mantooth, P. Weiss, and H.-J. Freund, "Interaction of CO molecules with surface state electrons on Ag(111)," *Surf. Sci.* **590**, L253–L258 (2005).